

# Single-cell resolution in high-resolution synchrotron X-ray CT imaging with gold nanoparticles

Elisabeth Schültke,<sup>a\*</sup> Ralf Menk,<sup>b</sup> Bernd Pinzer,<sup>c</sup> Alberto Astolfo,<sup>c</sup>  
Marco Stampanoni,<sup>c,d</sup> Fulvia Arfelli,<sup>e</sup> Laura-Adela Harsan<sup>f</sup> and Guido Nikkhah<sup>g</sup>

<sup>a</sup>Stereotactic and Functional Neurosurgery, Freiburg University Medical Center, Breisacher Strasse 64, Freiburg 79106, Germany, <sup>b</sup>Sincrotrone Trieste SCpA, Science Park, Trieste, Italy, <sup>c</sup>Swiss Light Source, Paul Scherrer Institute, Villigen, Switzerland, <sup>d</sup>Institute for Biomedical Engineering, University and ETH Zurich, Zurich, Switzerland, <sup>e</sup>Dipartimento di Fisica, Università di Trieste and Istituto Nazionale di Fisica Nucleare Sezione di Trieste, Trieste, Italy, <sup>f</sup>Medical Physics, Radiology Department, Freiburg University Medical Center, Freiburg, Germany, and <sup>g</sup>Neurochirurgische Klinik, Universitätsklinikum Erlangen, Schwabachanlage 6, 91054 Erlangen, Germany.

\*E-mail: elisabeth.schuelcke@uniklinik-freiburg.de

Gold nanoparticles are excellent intracellular markers in X-ray imaging. Having shown previously the suitability of gold nanoparticles to detect small groups of cells with the synchrotron-based computed tomography (CT) technique both *ex vivo* and *in vivo*, it is now demonstrated that even single-cell resolution can be obtained in the brain at least *ex vivo*. Working in a small animal model of malignant brain tumour, the image quality obtained with different imaging modalities was compared. To generate the brain tumour,  $1 \times 10^5$  C6 glioma cells were loaded with gold nanoparticles and implanted in the right cerebral hemisphere of an adult rat. Raw data were acquired with absorption X-ray CT followed by a local tomography technique based on synchrotron X-ray absorption yielding single-cell resolution. The reconstructed synchrotron X-ray images were compared with images obtained by small animal magnetic resonance imaging. The presence of gold nanoparticles in the tumour tissue was verified in histological sections.

**Keywords:** animal model; brain tumour; high-resolution imaging; gold nanoparticles; X-ray CT.

© 2014 International Union of Crystallography

## 1. Introduction

Advanced imaging methods like computer tomography (CT) and magnetic resonance imaging (MRI) belong to the standard methods for initial diagnostic and follow-up in patients with malignant brain tumours. The therapy recommendation is generally based on the overall condition of the patient and on the extent of infiltration of vital or/and eloquent cerebral structures. There is a high demand for the development of imaging methods with a high spatial resolution, which could help to better understand tumour development and response to therapy functionally and structurally. Positron tomography, for instance, is uniquely suited to visualize functional information. The spatial resolution, however, is only about 4–8 mm. With a two-point discrimination of less than 1 mm, MRI is currently the clinical imaging method with the best spatial resolution (Patel *et al.*, 2012). MRI can show intracerebral structures of human patients in three dimensions and in great detail. For the small animal models of malignant brain tumour that are frequently used to develop new therapeutic approaches, however, the spatial resolution of clinical MRI is insuf-

ficient. The size difference between the human brain and the brains of experimental animals spans more than one order of magnitude. Thus, a brain tumour in a human patient is often much larger than the entire brain in a small animal model. Where human brain tumours often have diameters of several centimetres, the diameters of brain tumours in small animals measure only a few millimetres. Researchers face a major challenge: the spatial resolution of the standard imaging methods available in the hospital environment is too low to render detailed images of the brain tumour in the small animal model comparable with that seen in human patients. Therefore, it can become difficult to assess the impact of experimental therapy on size changes and metastatic spread in a small animal model and to predict the response to the same therapy in human patients based on images acquired in small animal models. Dedicated devices like micro-CT and high-field small animal MRI, on the other hand, can show good anatomical detail even in the brain of small animals *in vivo*, but to the best of our knowledge not at cellular level in a mammalian organism (Paulus *et al.*, 2000; Heyn *et al.*, 2006; Badea *et al.*, 2008; Schambach *et al.*, 2010). Also, with image acquisition

times of more than 1 h duration, they present a challenge to animal care during a prolonged anaesthesia.

Especially with the MRI technique there have been efforts to develop cellular markers suitable for single-cell detection and long-term tracking of implanted cells. Although several work groups have addressed the pharmacodynamic and pharmacokinetic capacities of iron oxide particles, most of them aim at the use of the intravenous administration of these particles rather than the marking of single cells for the purpose of cell tracking (Ma *et al.*, 2012; Roohi *et al.*, 2012; Serrano-Ruiz *et al.*, 2012). In some studies, superparamagnetic iron oxide particles have been used as markers for MRI *in vivo* studies as well as in histological studies, where the iron oxide particles can be detected with a Prussian blue stain in histology sections (Schellenberger *et al.*, 2012). In the MRI studies where cells had been marked with iron oxide beads before cell implantation, the presence of the marked cells was observed as a void of varying size within the structure of the host brain (Jendelová *et al.*, 2004; Bulte *et al.*, 2010; Sandvig *et al.*, 2012). The marked cells, or rather the signal void as indirect indicator of their presence, can be detected in principle but the signals of two individual neighbouring cells cannot be resolved. The development of cell detection and tracking modalities that allow single-cell resolution in a reasonably short time could therefore have a high impact on the quality of preclinical imaging in small animal models.

We have recently shown that with synchrotron-based and micro-focus-tube-based CT taking advantage of edge enhancement, a very simple form of phase-contrast X-ray imaging, and gold nanoparticles (GNPs) as cell markers it is possible to detect small groups of implanted tumour cells in small animal models *ex vivo* and *in vivo* (Menk *et al.*, 2011; Astolfo *et al.*, 2013a,b). Mizutani *et al.* (2010) reported single-cell resolution with microtomography at a synchrotron in 2010, in small tissue blocks that were impregnated *ex vivo* with a silver stain, with the aim to highlight neuronal anatomy. The experiment described in this manuscript was designed to test the detection limit for tumours grown from GNP-loaded implanted cells with high-resolution local tomography using synchrotron-based X-ray imaging and compare the acquired images with those obtained with conventional CT and small animal MRI.

## 2. Material and methods

### 2.1. Cell culture and animal model

**2.1.1. Preparing GNP.** Colloidal GNPs (~50 nm diameter) were prepared as described originally by Frens and outlined previously (Frens, 1973; Juurlink & Devon, 1991). Briefly, 400 ml of 0.01% HAuCl<sub>4</sub> (Sigma) was boiled for 5 min, after which 4.0 ml of 1% sodium citrate was quickly added and the fluid was kept boiling for 30 min more. After cooling the fluid down on ice, 3 ml of sterile potassium carbonate (K<sub>2</sub>CO<sub>3</sub>) was added; the resulting pH was 5.5. Finally, 1 ml dialyzed horse serum was slowly added. The solution was then centrifuged at 10000 r.p.m. for 30 min. The supernatant was aspirated and the

pellet was re-suspended in 400 ml sterile water, followed by a second round of centrifugation. The resulting pellet was re-suspended in 20 ml of the growth medium for C6 glioma cells (DMEM, 10% FBS + 2 mM pyruvate + 15 mM glucose + 15 mM sodium bicarbonate + 2 mM glutamine) to form a GNP stock. A concentration of about 464 µg ml<sup>-1</sup> of elemental gold was determined by mass spectroscopy. The gold stock was frozen in aliquots for subsequent use. The size of the GNP is controlled by the amount of sodium citrate added during the nucleation process, in our case about 50 nm diameter (Juurlink & Devon, 1991).

**2.1.2. Loading C6 glioma cells with GNP.** C6 glioma cells (ATCC, USA) were seeded in 100 mm culture dishes and grown in a humidified incubator at 37°C with 5% CO<sub>2</sub>. When they were about 70% confluent, 1 ml of gold stock was added to the growth medium of each 100 mm culture dish to make up a final volume of 9 ml with a concentration of about 52 µg ml<sup>-1</sup> of elemental gold. The C6 glioma cells were harvested 22 h later using a Ca<sup>2+</sup>/Mg<sup>2+</sup>-free balanced salt solution containing 0.3 mM ethylene diamine tetra acetic acid (EDTA), 2 mM pyruvate, 7.5 mM glucose 15 mM NaHCO<sub>3</sub> and 15 mM HEPES buffer (pH 7.2). About 10<sup>6</sup> C6 cells ml<sup>-1</sup> were suspended in Hank's balanced salt solution and kept on ice until implantation.

**2.1.3. Tumour cell implantation.** The C6 glioma in adult Wistar rats is a frequently used small animal model to test new diagnostic and therapeutic approaches for the malignant human brain tumour glioblastoma multiforme. With the animal under general anaesthesia, 1 × 10<sup>5</sup> gold-loaded C6 glioma cells were injected into the anterior aspect of the right cerebral hemisphere of an adult male Wistar rat (324 g), about 3 mm below the cortical surface. After the tumour cell injection, the animal was allowed to recover, being housed and cared for in a temperature-regulated animal facility exposed to a 12 h light/dark cycle. The experiment was performed in accordance with the guidelines of the German Councils on Animal Care. The study was specifically approved by the Institutional Animal Care and Use Committee at the Freiburg University Medical Center. The animal was sacrificed under deep isoflurane anaesthesia 16 days after the tumour cell implantation and the head was removed.

### 2.2. Synchrotron-radiation-based CT image acquisition

Images were acquired at the TOMCAT beamline of the Swiss Light Source (SLS; Stampanoni *et al.*, 2007) and at the SYRMEP beamline of Elettra Sincrotrone Trieste (Tromba *et al.*, 2010), third-generation synchrotron facilities operating at an electron energy of 2.4 GeV and 2.0 GeV at ring currents of 400 mA and 200–300 mA, respectively. The head was mounted upright in a tight plastic cylinder of 20 mm diameter containing 10% phosphate-buffered formalin. At the SLS a double-bounce multilayer monochromator was used to select the desired energy from the emission spectrum of the 2.9 T bending magnet. An approximate of the volume-averaged dose for the overview scan can be carried out by determining the fraction of absorbed photons from the flat-field-corrected

radiographic projections (about 70% on average). The impinging flux was about  $7 \times 10^{10}$  photons  $\text{s}^{-1} \text{mm}^{-2}$ , which corresponds to a dose rate of  $10 \text{ Gy s}^{-1}$ , which was determined by means of a silicon PIN diode. As X-ray detector a  $20 \mu\text{m}$  LuAG scintillator was used, coupled *via* exchangeable objectives to a CCD camera (PCO.2000, PCO AG, Germany). For the acquisition of scout images a magnification of  $1.25\times$  was used, yielding a pixel size of  $5.92 \mu\text{m} \times 5.92 \mu\text{m}$  and a field of view (FOV) of  $12.1 \text{ mm} \times 12.1 \text{ mm}$ . A total of 6000 angular projections over  $360^\circ$  were acquired, with an exposure time for each frame of 160 ms resulting in a total acquisition time of 16 min. An energy of 22 keV was selected because of the strong absorption of the bone. Based on the overview scan, the coordinates of the tumour cells were calculated, and a local tomography scan with  $20\times$  magnification (pixel size  $0.37 \mu\text{m} \times 0.37 \mu\text{m}$ , FOV  $750 \mu\text{m} \times 750 \mu\text{m}$ , exposure time 120 ms, 2500 tomographic projections) was carried out at the position of the tumour. Data were acquired over  $180^\circ$  with an angular step size of  $0.072^\circ$ . The entrance dose in this case was approximately 4 kGy. The tomographic data sets were reconstructed using the TOMCAT processing pipeline with in-house software on a Linux cluster (Hintermüller *et al.*, 2010). At the SYRMEP beamline a photon energy of 24 keV (0.1% bandwidth) with an average photon fluence of  $\sim 1 \times 10^8$  photons  $\text{s}^{-1} \text{mm}^{-2}$  measured on entrance to the sample was used. Propagation-based phase-contrast images were collected at a sample-to-detector distance of 80 cm. The X-ray detector employed is a commercially available phosphor fibre-optic coupled CCD with  $14 \mu\text{m} \times 14 \mu\text{m}$  pixel size and a spatial resolution of about  $30 \mu\text{m}$  (full width at half-maximum of the point spread function) (Photonic Science, Hystar X-ray imager, East Sussex, UK). The active area of the CCD ( $28 \text{ mm} \times 28 \text{ mm}$ ) and the vertical beam size (4 mm) governs a FOV of  $28 \text{ mm} \times 4 \text{ mm}$ . The pixel depth is 16 bit. The exposure times ranged from 4–10 s per projection depending on the synchrotron machine current. A total of 900 projections were acquired equiangularly over  $180^\circ$ . This resulted in an entrance dose in air of about 5 Gy. The dark- and flat-field corrected projection data were phase retrieved and reconstructed using the XTRACT package setting  $\delta/\beta = 14.81$  for gold at 24 keV. For the latter the slice data are given in terms of  $\beta$  which can be converted into linear attenuation values by simple multiplication ( $\mu = k\beta$ , with  $k$  the length of the wavevector). Slice data were analysed, manipulated and rendered using the Osirix software package (<http://www.osirix-viewer.com>; Geneva, Switzerland), Drishti (<http://anusf.anu.edu.au/Vizlab/drishti/>) and ImageJ (<http://rsb.info.nih.gov/ij/>; Bethesda, USA). The histogram analysis was carried out using the multi-peak-fitting plugin (version 2) of IGOR version 6.31 (<http://www.wavemetrics.com/index.html>).

### 2.3. Magnetic resonance image acquisition

Data were acquired on a 9.4 T BioSpec MRI scanner system with BGA12S gradients (Bruker BioSpin GmbH, Karlsruhe, Germany). The  $T_2^*$ -weighted sequences used were susceptibility weighted imaging (SWI) with an echo time  $TE = 20 \text{ ms}$

and repetition time  $TR = 861 \text{ ms}$  and three-dimensional fast low-angle shot (FLASH) with  $TE = 10 \text{ ms}$ ,  $TR = 34 \text{ ms}$  and flip angle  $\alpha = 30^\circ$ .

$T_2$  relaxation depends on the presence of static internal fields within the head stemming from protons on larger molecules. The superposition with the external magnetic field generates local field non-uniformities and subsequently causes the protons to progress at slightly different frequencies, which results in  $T_2^*/T_2$  relaxation subsequent to a perpendicular radiofrequency (RF) pulse. Thus  $T_2^*/T_2$  is the relaxation time required to regain transversal magnetization following an RF pulse. In general, darkness in magnetic resonance (MR) images depends on the density of protons in that area whereas an increased density is associated with darker shades in the MR image. Normally, fat, water and fluid are rendered bright while bone would appear dark. Due to the increased density of protons, GNPs, but also hemorrhages featuring a high Fe concentration, are rendered dark. Tumour is brighter than white matter, which renders brighter than grey matter in  $T_2$ -weighted images; therefore,  $T_2$ -weighted imaging is ideal for picking up differences in brain tissue and tumours. The voxel was an isotropic cube of  $60 \mu\text{m}$  side and the FOV was  $15.3 \text{ mm} \times 11.9 \text{ mm} \times 15.3 \text{ mm}$  using an acquisition time of about 14 h. The images were converted to DICOM format and reconstructed using IMPAX EE software VIII (AGFA Healthcare, Mortsels, Belgium).

### 2.4. Histology

At the end of the imaging experiments, the brain was dissected out of the skull and two  $\sim 4 \text{ mm}$ -thick coronal slices containing tumour were embedded in paraffin. Sections of thickness  $5 \mu\text{m}$  were mounted on microscopy slides and stained according to a haematoxylin–eosin (H&E) standard protocol. Haematoxylin stains nuclei of cells blue. Due to their high cell density, malignant tumours appear intensely blue. Eosin stains eosinophilic structures in various shades of red and pink. Erythrocytes (red blood cells) are stained intensely red.

## 3. Results

### 3.1. Image acquisition at the synchrotron

Overview (scout) images (Fig. 1) and phase-retrieved images (Fig. 2) allowed both a larger tumour around the tumour cell implantation site and a second smaller tumour right temporal to be identified. Already in these ‘low-resolution’ images, small clusters (aggregates) of cells marked with GNP were identified. Soft tissue structures not enhanced by GNP were not visible in the CT images. The images reconstructed from data acquired in local tomography mode are shown in Figs. 3 and 4. For the latter, some individual cells have also been reconstructed both from the post-mortem sample and from cells suspended and imaged in 2% agar. The size of those individual cells corresponds both in size and shape to the parameters of this type of tumour cell seen in cell culture studies. The rugged outer contour of the reconstructed

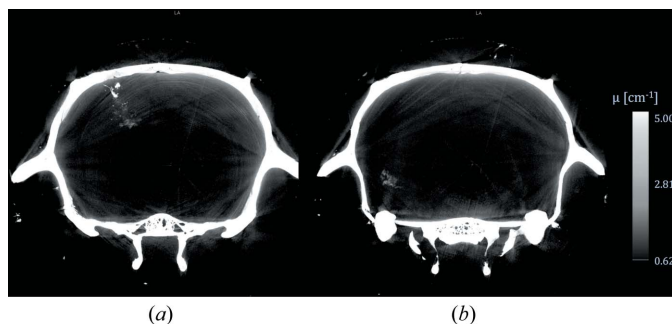


**Figure 1**  
Maximum intensity projection (MIP) over ten subsequent coronal slices reconstructed from the TOMCAT synchrotron phase-contrast CT data. Slice thickness was scaled to the slice thickness of MR images. Both the larger tumour around the site of cell implantation (a) and a smaller tumour in right temporal position (b) can be seen in the right cerebral hemisphere.

tumour corresponds to that seen in the surface of the reconstructed single cells. Having seen larger GNP clusters already in the overview or scout images, in the local tomography images we were able to identify individual clusters (aggregates) (Fig. 3). Measured at high magnification, the distances between the individual cell clusters ranged between less than 2.5 up to 60  $\mu\text{m}$ .

The morphological structures invaded by the tumour can be appreciated when the CT images are overlaid by a corresponding MR image, as shown in Figs. 7 and 8. The void created by the GNP in the MRI image is larger than the volume marked by GNPs. This could be due to two reasons separately or in combination. It is possible that the void generated by GNPs in the MR image is larger than the actual volume of the GNPs. On the other hand, cells with very low GNP content might not be sufficiently opaque to be detected with the X-ray imaging method. Also, part of the tumour might have already become necrotic, as is typical for this type of tumour. This was actually later verified in the histology sections. The necrotic cells would be removed by macro-

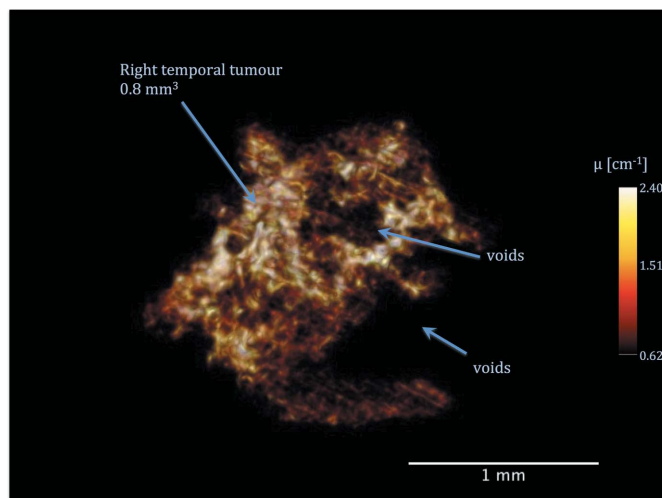


**Figure 3**  
Three-dimensional rendering of the right temporal tumour (voxel  $14\ \mu\text{m} \times 14\ \mu\text{m} \times 14\ \mu\text{m}$ ). Display settings: lower threshold  $\mu_{\text{min}} = 0.62\ \text{cm}^{-1}$ , upper threshold  $\mu_{\text{max}} = 2.4\ \text{cm}^{-1}$ .

phages. The GNP could either have been likewise removed by macrophages or taken up by the neighbouring tumour cells.

Both the larger tumour at the implantation site and a smaller secondary tumour in right temporal position are shown. As expected from X-ray CT the morphology of bones is displayed with great detail in the three-dimensional renderings of the overview image (Fig. 2). Morphological features such as skull sutures and the burr hole through which the cells were implanted are prominent. The spongy bone that separates the two compact bone plates of the skull can also be identified but soft tissues are mainly invisible. Brain tissue is not enhanced with the contrast settings used in this rendering (lower threshold  $\mu_{\text{min}} = 0.62\ \text{cm}^{-1}$  and upper threshold  $\mu_{\text{max}} = 5\ \text{cm}^{-1}$ ). Owing to the contrast enhancement of the GNP the tumour that developed in this animal features

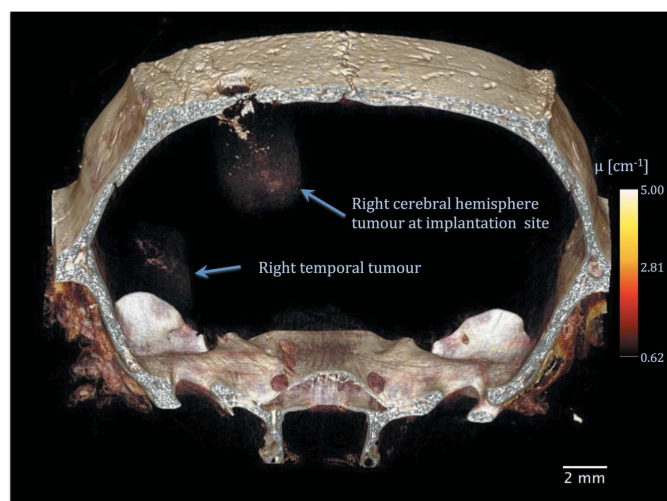


**Figure 2**  
*XTRACT* phase-retrieved coronal CT image reconstructed from the SYRMEP data, 5 mm thick.

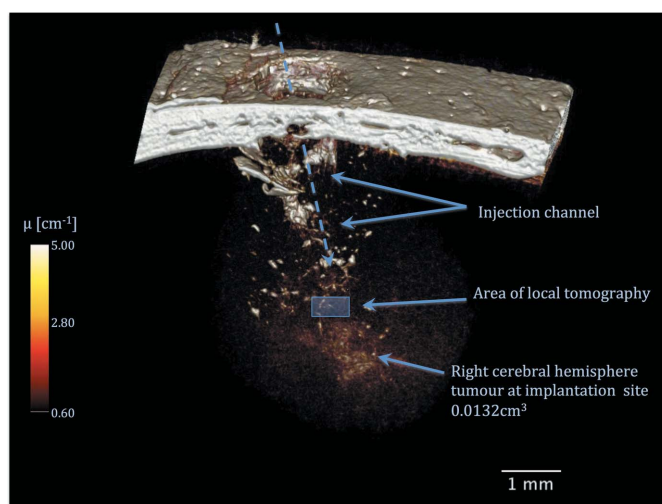


**Figure 4**  
Three-dimensional rendering of the primary tumour (voxel size  $14\ \mu\text{m} \times 14\ \mu\text{m} \times 14\ \mu\text{m}$ ). Display settings: lower threshold  $\mu_{\text{min}} = 0.60\ \text{cm}^{-1}$ , upper threshold  $\mu_{\text{max}} = 5\ \text{cm}^{-1}$ .

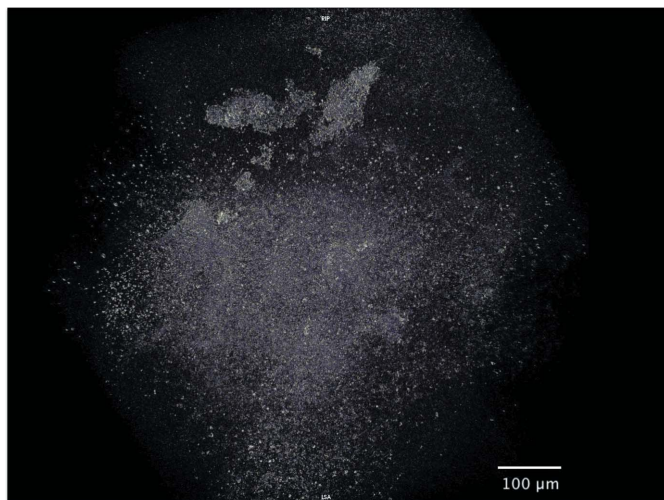


**Figure 5**  
Local tomography of a part of the primary tumour, synchrotron-based CT, corresponding to the blue rectangle indicated in Fig. 4. Angular step size 0.072°, data acquisition over 180°.

two well distinguishable lesions: a larger tumour around the tumour cell implantation site and a second smaller tumour right temporal. The infiltrating nature of the malignant brain tumour is evident in the right temporal tumour (Fig. 3) with finger-like extensions of tumour cells extending from the main bulk of the tumour. Smaller and larger voids within the tumour mass are noticeable as indicated by the arrows in Fig. 3.

The voids represent the absence of cells with a content of GNPs sufficient to be detected. This could be due either to a necrotic tumour part, which is typical for a glioblastoma, or because the cells have been through a higher number of mitotic cycles and therefore the gold contents of individual cells is below the detection limit. Bone debris can be identified from the burr hole downwards along the injection channel at the injection site of the primary tumour (Fig. 4) in the right cerebral hemisphere. Approximately 3 mm below the cortical surface, corresponding to the cell implantation site, a compact high-absorbing mass of about 0.0132 cm<sup>3</sup> volume can be identified. This mass is surrounded by a halo of low-absorbing material ( $\mu \approx 0.60 \text{ cm}^{-1}$ ). Some brighter and small-sized details ( $\mu \approx 1.60 \text{ cm}^{-1}$ ) can be observed within the tumour mass as well.

The rendering of the local CT (local tomography, Fig. 5) displays the high-resolution morphology of X-ray opaque objects in a region of interest (ROI) within the larger lesion in the right cerebral hemisphere. The overall volume of the ROI is about 0.4 µm<sup>3</sup> and

coincides with the blue shaded region indicated in Fig. 4. Depending on the image reconstruction, the inherent spatial resolution of approximately 1 µm × 1 µm (at a pixel size of 0.37 µm × 0.37 µm) of the nano CT system is sufficient to reveal small cell groups or even single cells with an expected cell diameter of about 10 µm. This fact is supported by distances between individual GNP clusters shorter than 2.5 µm. Since our CT imaging method does not allow us to see any cellular structures but only to pick up the signal enhancement caused by the gold component of the GNP, it is not possible to group the GNP clusters belonging to individual cells. From the scanning electron microscopy study quoted earlier we know that the distances between GNP clusters inside a cell are in the range 0.2–8 µm. Larger distances between GNP clusters were seen in the area of the cellular nuclei, because GNP were never observed inside a nucleus. In our current study we can distinguish individual GNP clusters with distances between the clusters of about 1 µm. Thus, it is highly likely that more than one GNP cluster belongs to one individual cell. This means that single-cell resolution has been obtained.

Several spherical structures with different absorption properties can be recognized. Due to the reasonable signal-to-noise ratio of the spherical structures in the slice data (Fig. 6a), image segmentation using the three-dimensional neighbourhood growing region plugin of the *Osirix* software allows the cells to be rendered without the aerosol-like background and the physical dimensions of the spheres to be accessed. Fig. 6(a) shows the result of the segmentation within one CT slice. The sphere on the right is cross-sectioned approximately in its

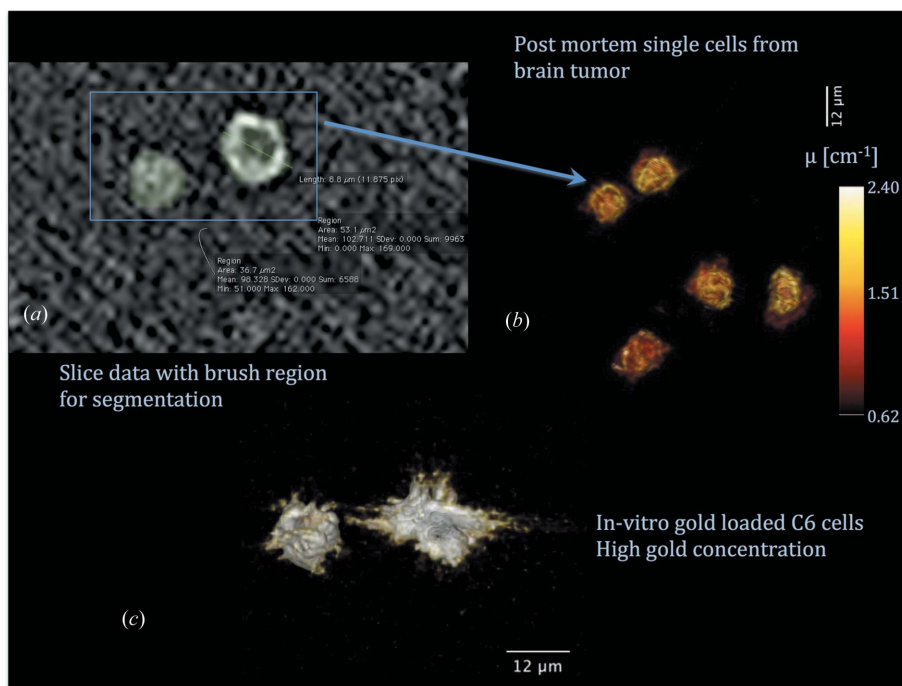


**Figure 6**  
Segmented (a) and reconstructed (b) image of individual gold-loaded cells. Diameters of the cell bodies are between 8 and 10 µm. (c) Reconstructed image of GNP-loaded cells *in vitro*. The reconstructed image of the second, smaller, tumour in Fig. 4 shows the same rugged surface as seen in the GNP-loaded cells.

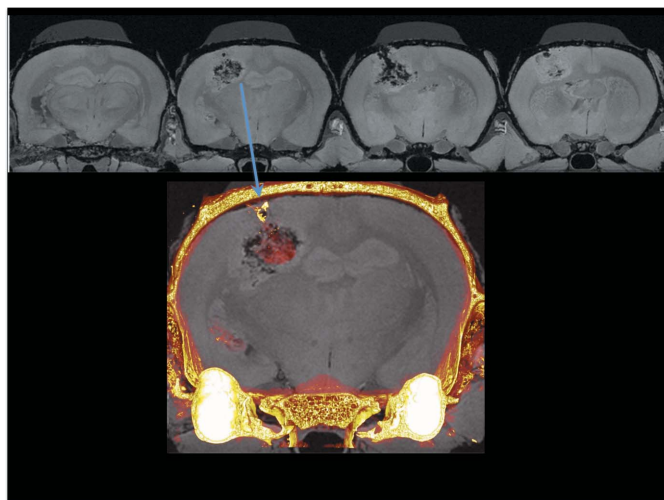


**Figure 7**  
High-resolution coronal  $T_2^*$ -weighted MR images of the rat brain. Subsequent high-resolution axial slices (resolution  $60\ \mu\text{m} \times 60\ \mu\text{m} \times 60\ \mu\text{m}$ ) showing the main bulk of the tumour in the right hemisphere as a dark void caused by the GNPs and the small haemorrhages typical for a high grade glioma. A coronal slice of the CT scout image was overlaid with a corresponding MRI slice.

middle plane. The diameter of this sphere is about  $9\ \mu\text{m}$ . The three-dimensional rendering reveals that only the outer regions close to the spheres' surfaces possess absorption properties. A central region of reduced absorption is prominent, most likely corresponding to the nucleus of the cell (free of GNP). Once segmented, the volume of the brushed regions and thus of the spheres can be assessed. The mean of the five spheres shown in Fig. 6(b) is  $640 \pm 90\ \mu\text{m}^3$ . The size of those

individual cells corresponds both in size and shape to the parameters of this type of tumour cell seen in cell culture studies.

### 3.2. MR image acquisition

The invasive nature of the tumour is evident both in the MRI images and in the fused MRI-CT images. Both the larger and the smaller tumour were visible in morphological  $T_2^*$ -weighted MR images obtained using a three-dimensional FLASH sequence (Figs. 7 and 8). The isotropic resolution of the MR images ( $60\ \mu\text{m} \times 60\ \mu\text{m} \times 60\ \mu\text{m}$ ) allowed the image reconstructions in coronal (Fig. 7) and axial orientations (Fig. 8). Dark voids surrounded by soft tissue are visible within the tumour matrix (see the enlarged view in Fig. 7). Although those voids could be partially caused also by the small haemorrhages seen in the histology, we assume that much of this phenomenon is generated by the GNP aggregates within the tumour. Typical for a fast-growing space-occupying lesion, the right-sided tumour causes a shift of the midline structures towards the left side.

### 3.3. Histology

In the photograph of the complete coronary section, both tumours can be identified on the right-hand side (Fig. 9). As in the MRI images, the compression and the midline shift of normal structures caused by the space-occupying lesion towards the left are clearly visible. The microscopy images show the typical features of a fast-growing malignant glial tumour, namely a high density of cells, mitotic figures,

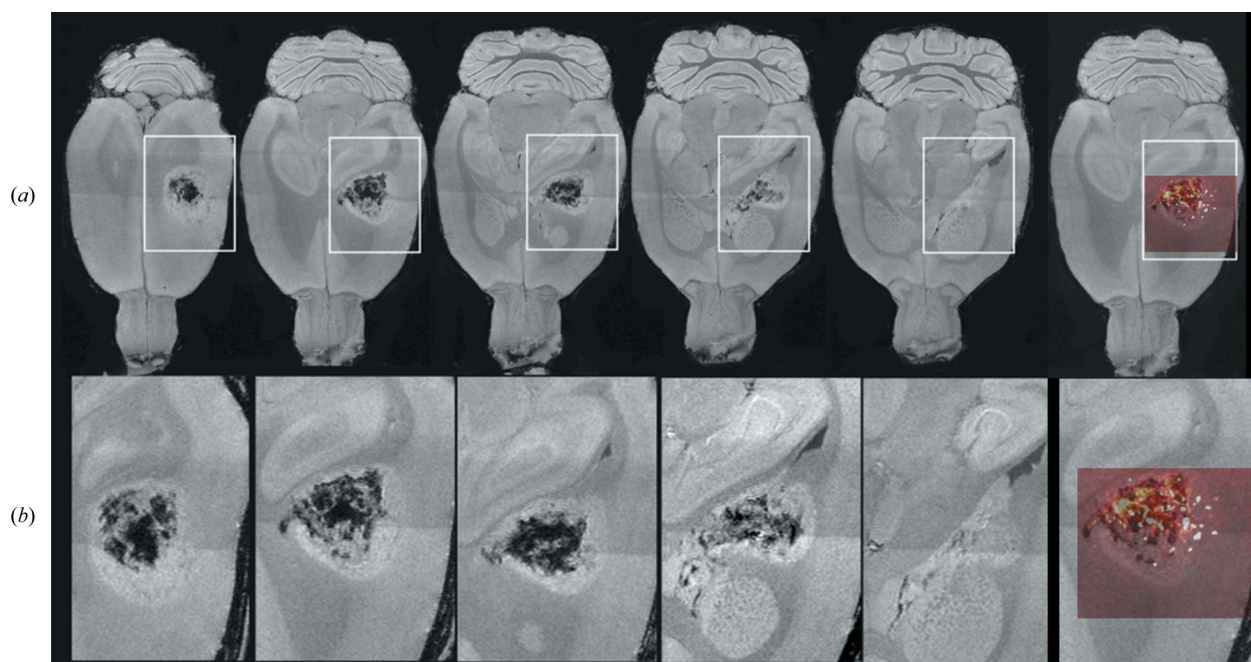


**Figure 8**  
High-resolution axial  $T_2^*$ -weighted MR images of the rat brain (three-dimensional FLASH sequence). Axial brain sections acquired with high isotropic resolution ( $60\ \mu\text{m} \times 60\ \mu\text{m} \times 60\ \mu\text{m}$ ). The visible hypo-intense areas correspond to GNP aggregates and small haemorrhages within the soft tissue structure of the tumour (a). Enlarged views of the tumours sites are provided in (b). An axial slice of the CT scout image was overlaid with a corresponding MRI slice.

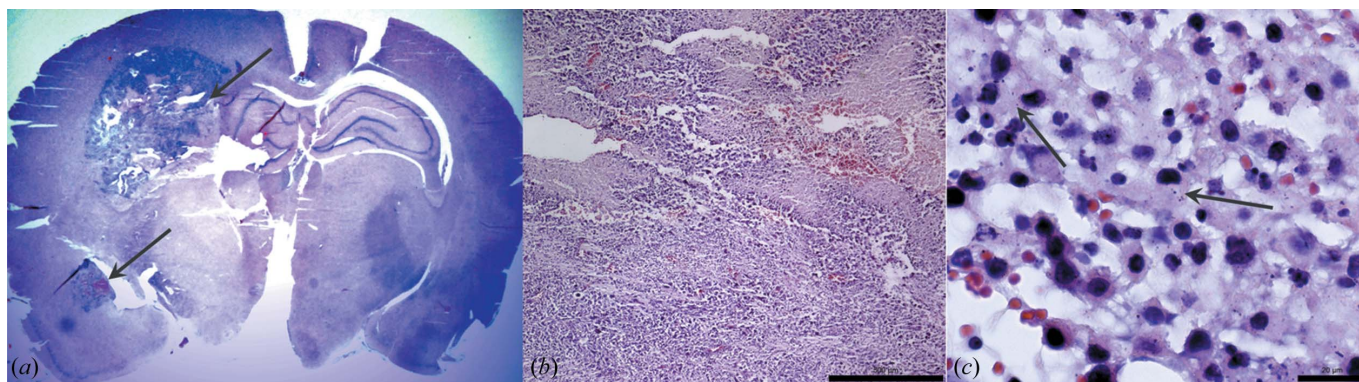


**Figure 9**

H&E stained coronal histology section of the rat brain. Overview over the entire brain, showing both tumours in the right hemisphere, indicated by arrows (a). Enlarged microscopy images showing typical features of the larger tumour (b and c). GNPs are recognizable as small black dots on high-magnification micrographs (some are indicated by arrows). Section thickness: 5  $\mu\text{m}$ .

neovascularization, haemorrhage and necrosis. GNPs are seen on the enlarged microscopy images.

#### 4. Discussion

Correlating the three-dimensional CT reconstructions with the findings from MRI and histology allows the following interpretation of the biological picture: typical for the environment of a burr hole in the skull, the injection channel and the implantation site in the ROI depicted in Fig. 4, we encounter residual bone debris close to the burr hole, which can be identified as small sized (particle size 2–7  $\mu\text{m}$ ) and highly absorbing objects. For cells of the first generation that never underwent mitosis, the initial gold concentration would be transferred. An alternative explanation for some of those small and highly absorbing objects would be macrophages which have incorporated the entire gold content of a GNP-loaded cell that has never proliferated and therefore still contains the entire original gold load.

The spherical structures with diameters of about 10  $\mu\text{m}$  shown in Fig. 6 can be identified as GNP-loaded tumour cells in an environment of tumour haemorrhage and possibly free GNP clusters. The measured volume of  $640 \pm 90 \mu\text{m}^3$  is about 20% smaller than the cell volume reconstructed from *in vitro* studies of C6 cells suspended in 2% agar (Fig. 6c) and imaged with the TOMCAT set-up (Astolfo *et al.*, 2013b). The volume of the cells measured *in vitro* corresponds to that reported from other *in vitro* studies (Staub *et al.*, 1990). The size differences between the cells measured *in vitro* and those measured *in situ* can be explained by the different environment in which these cells exist.

In the histology sections, the C6 cells are between 12 and 20  $\mu\text{m}$  long and measure between 6 and 12  $\mu\text{m}$  at the widest circumference at the part of the cell body containing the nucleus. Using scanning electron microscopy we had shown earlier that GNPs were present in the cells in multiple small clusters (aggregates) and are stored in lysosomes of the C6 cells (Astolfo *et al.*, 2013b). GNPs were never observed inside a nucleus. Therefore GNP-loaded C6 cells should be rendered

as hollow spheres or ellipsoids in the CT, which in fact is confirmed in Fig. 6.

It is noteworthy that the cells shown in Fig. 6 have different absorption values, which indicates a difference in GNP content. As shown previously (Astolfo *et al.*, 2013b), the concentration of GNPs decreases with each mitotic cycle since the gold is divided between the daughter cells. It is therefore a sensitive assumption that these cells are progenies of the original cell graft. The question of how many mitotic cycles these cells have accomplished can be assessed by analysing the distribution of the linear absorption coefficient of the tumours. The larger tumour can be described with three Gaussian peaks on a constant background, where the first peak represents the image background, the second peak represents the gold-loaded cells and the third peak represents the bone debris. Two peaks can approximate the second, smaller, tumour, one representing the background and the other representing the gold-loaded cells. Since the linear absorption coefficient is proportional to the gold concentration, this helps us to obtain some information on the cell proliferation. The background in the larger tumour and in the second smaller tumour is at  $\mu_{\text{min}} = 0.58 \pm 0.02 \text{ cm}^{-1}$  and  $0.59 \pm 0.02 \text{ cm}^{-1}$ , respectively. The peak of the GNP-loaded cells is situated at  $0.81 \pm 0.05 \text{ cm}^{-1}$  for the larger and at  $0.79 \pm 0.04 \text{ cm}^{-1}$  for the smaller tumour. This indicates that the gold concentration should be similar in both tumours. Thus, it is highly likely that the smaller right temporal tumour was generated from some of the original GNP-loaded cells migrating to this location actively from the implantation site rather than being a later metastasis broken off from the larger tumour.

A known disadvantage of X-ray tomography is the lack of structural detail in most soft tissues not containing contrast agent or specific markers. This is true for both conventional CT and synchrotron-based CT. The distinction of soft tissue detail is much easier in MRI scans. However, the CT scan offers a great advantage over MRI: based on X-rays, the CT images are geometrically correct, while this is not true for MRI images due to the image reconstruction from electromagnetic field gradients. For this reason the advantages of both techniques are often combined where exact target loca-

lization is required in the clinical setting, similar to the overlay shown in Figs. 7 and 8.

The spatial resolution obtained with clinically available CT scanners is far from the requirements for imaging in small animal models of human disease. Thus, special dedicated imaging devices should be used. We have shown in our experiments that synchrotron-based X-ray CT provides the necessary spatial resolution to identify single cells in *ex vivo* studies.

One of the challenges on the way to using synchrotron-based X-ray CT imaging for single-cell resolution *in vivo* is to modify the image acquisition process so that the X-ray exposure can be reduced to levels which are acceptable for longitudinal studies with repeated follow-up imaging. In our previous study (Astolfo *et al.*, 2013a) we have shown that *in vivo* imaging of cell clusters with X-rays is feasible at entrance doses in air of the order of 100 mGy. Imaging experiments of single cells with a 24 keV monochromatic synchrotron beam have been previously reported where animals were exposed to (effective) doses of more than 10 Gy in one single imaging experiment (Bayat *et al.*, 2005). Using monochromatic beam, Chien *et al.* (2012) recently reported single-cell resolution *in vivo* augmented by microvascular studies, using doses of about 34 Gy for the acquisition of one single CT image, acquiring several images per animal to follow the dynamics of the contrast agent. However, such high doses would not be acceptable for repeated follow-up imaging in a tumour therapy experiment. Effective doses of 2 Gy and higher are typically applied as one single fraction in a series of temporally fractionated radiotherapy in patients with malignant brain tumours (Stupp *et al.*, 2005). Thus, one would expect that a repeatedly conducted imaging process which exposes the tumour-bearing animal to doses of 2 Gy or higher would interfere with the therapeutic experiment it is supposed to monitor. Those are values for white-beam irradiation. A pilot experiment in C6 cell cultures after exposure to a single dose of 0.5 Gy of 24 keV monochromatic beam suggested that some DNA double-strand breaks did occur (Schültke *et al.*, 2010).

GNPs are sequestered in the lysosomes after uptake in the cells and are thought to be biologically inert (Devon & Juurlink, 1989). Stability and biocompatibility of GNPs have also been investigated by others (Staub *et al.*, 1990). However, gold as a high-*Z* element has the capacity to increase the absorption of X-ray energy and subsequently may cause some damage in the gold-loaded cells, compared with naive cells. Thus, the next logical step would be to conduct a series of biodosimetry studies. This should be done by looking at transplants of both naive and GNP-loaded cells following single as well as repeated image acquisition with monochromatic beam in small animal models of human disease. Thus, it should be determined whether single-cell resolution can be used to follow up disease development in small animal models. For *ex vivo* studies our technique can be used already as a non-destructive assessment method to deliver valuable three-dimensional information about migration and distribution of implanted cells at the endpoint of a study.

Small animal MRI (high-field scanners) can deliver high-quality images when relatively long anaesthesia times are acceptable. Preclinical studies have shown that the anatomical information generated by MRI can be enhanced by intravenous administration of superparamagnetic iron oxide nanoparticles (Guimaraes *et al.*, 2011; Roohi *et al.*, 2012). In this case, however, enhancement is either selectively vascular or based on the break down of vascular barriers rather than being representative of cell-specific imaging. MRI of single cells loaded with superparamagnetic iron oxide particles has been shown in cell cultures (Bakhrū *et al.*, 2012). When bone-marrow-derived stem cells loaded with iron oxide particles were transplanted into a small animal model, however, cerebral MRI showed major voids created by the particles. Single cells were not identifiable (Jendelová *et al.*, 2004). In our MRI images, the C6 glioma grown from C6 cells loaded with GNPs also created larger voids in the brain matrix.

In an interesting study assessing the influence of particle size and coating of intravenously injected superparamagnetic iron oxide particles on the relaxivity of the MR signal and on the blood clearance, Roohi *et al.* (2012) found that the relaxivity increased proportionally with increasing particle size up to a diameter of 60 nm and remained constant for larger particles. They also found that the coating of the iron oxide particles influenced the blood kinetics but there was little effect of the coating material on the image quality. In our study, blood clearance was not an issue because the GNPs were permanently enclosed in the lysosomes of the implanted tumour cells. Particle size, however, could be an interesting parameter where MRI is used as a well established imaging method either to interpret findings from the synchrotron-based CT in the development phase of the technique or to fuse CT and MRI images in order to combine the advantages of both imaging techniques, *i.e.* the geometrically correct data set of the synchrotron-based X-ray CT with single-cell resolution and the MRI data set with a detailed representation of soft tissue structures. The advantages of such image fusion concepts are regularly used with DICOM-based image formats in the clinical setting, to plan stereotactic neuro-surgical procedures. If our synchrotron imaging technique would pass the suitability test for small animal models of transplantation surgery in neurodegenerative diseases, it would be worthwhile to develop an image fusion approach for synchrotron CT and small animal MRI, possibly based on already existing software from the clinical setting. It might be sufficient to acquire MRI images once or twice during the entire observation period and fuse them with the more often acquired synchrotron CT images, in order to follow cell migration and possibly proliferation. In this case, it would be worthwhile to test whether there is a correlation between particle size and MRI relaxivity for GNPs, similar to that observed for iron oxide particles, and whether the 50 nm diameter of our GNPs might already be close to optimal for the purpose of MRI. It has been shown that particle size can be regulated by the concentration of sodium citrate in the chlorauric acid solution during the production process of GNPs (Frens, 1973). Thus, provided there is no significant

interference with cell function, we could prepare GNPs with optimal size for both cellular function, synchrotron-based X-ray CT and MRI.

The experiment at the SLS was conducted with support from the European Union (travel grant). ES holds a Marie-Curie-Reintegration Grant (FP 7, European Union); the sponsor had no role in the design of this study.

## References

- Astolfo, A., Arfelli, F., Schültke, E., James, S., Mancini, L. & Menk, R. H. (2013b). *Nanoscale*, **5**, 3337–3345.
- Astolfo, A., Schültke, E., Menk, R. H., Hall, C., Kirch, R., Stebel, M., Harsan, L., Juurlink, B. H. J. & Arfelli, F. (2013a). *Nanomedicine*, **9**, 284–292.
- Badea, C. T., Drangova, M., Holdsworth, D. W. & Johnson, G. A. (2008). *Phys. Med. Biol.* **53**, R319–R350.
- Bakhru, S. H., Altiok, E., Highley, C., Delubac, D., Suhan, J., Hitchens, T. K., Ho, C. & Zappe, S. (2012). *Int. J. Nanomed.* **7**, 4613–4623.
- Bayat, S., Apostola, L., Bollera, E., Brochard, T. & Peyrin, F. (2005). *Nucl. Instrum. Methods Phys. Res. A*, **548**, 247–252.
- Bulte, J. W. M., Engberink, R. D. O., van der Pol, S. M. A., Walczak, P., van der Toorn, A., Viergever, M. A., Dijkstra, C. D., de Vries, H. E. & Blezer, E. L. A. (2010). *Mol. Imag.* **9**, 268–277.
- Chien, C. C., Chen, H. H., Lai, S. F., Hwu, Y., Petibois, C., Yang, C. S., Chu, Y. & Margaritondo, G. (2012). *Sci. Rep.*, **2**, 610.
- Devon, R. M. & Juurlink, B. H. (1989). *Glia*, **2**, 266–272.
- Frens, G. (1973). *Nat. Phys. Sci.* **241**, 20–22.
- Guimaraes, A. R., Ross, R., Figueredo, J. L., Waterman, P. & Weissleder, R. (2011). *Mol. Imaging Biol.* **13**, 314–320.
- Heyn, C., Ronald, J. A., Ramadan, S. S., Snir, J. A., Barry, A. M., MacKenzie, L. T., Mikulis, D. J., Palmieri, D., Bronder, J. L., Steeg, P. S., Yoneda, T., MacDonald, I. C., Chambers, A. F., Rutt, B. K. & Foster, P. J. (2006). *Magn. Reson. Med.* **56**, 1001–1010.
- Hintermüller, C., Marone, F., Isenegger, A. & Stampanoni, M. (2010). *J. Synchrotron Rad.* **17**, 550–559.
- Jendelová, P., Herynek, V., Urdžíková, L., Glogarová, K., Kroupová, J., Andersson, B., Bryja, V., Burian, M., Hájek, M. & Syková, E. (2004). *J. Neurosci. Res.* **76**, 232–243.
- Juurlink, B. H. & Devon, R. M. (1991). *Experientia*, **47**, 75–77.
- Ma, Q., Nakane, Y., Mori, Y., Hasegawa, M., Yoshioka, Y., Watanabe, T. M., Gonda, K., Ohuchi, N. & Jin, T. (2012). *Biomaterials*, **33**, 8486–8494.
- Menk, R. H., Schültke, E., Hall, C., Arfelli, F., Astolfo, A., Rigon, L., Round, A., Ataellmannan, K., MacDonald, S. R. & Juurlink, B. H. (2011). *Nanomedicine*, **7**, 647–654.
- Mizutani, R., Takeuchi, A., Uesugi, K., Takekoshi, S., Osamura, R. Y. & Suzuki, Y. (2010). *Cereb. Cortex*, **20**, 1739–1748.
- Patel, V., Papineni, R. V., Gupta, S., Stoyanova, R. & Ahmed, M. M. (2012). *Radiat. Res.* **177**, 483–495.
- Paulus, M. J., Gleason, S. S., Kennel, S. J., Hunsicker, P. R. & Johnson, D. K. (2000). *Neoplasia*, **2**, 62–70.
- Roohi, F., Lohrke, J., Ide, A., Schütz, G. & Dassler, K. (2012). *Int. J. Nanomed.* **7**, 4447–4458.
- Sandvig, I., Thuen, M., Hoang, L., Olsen, Ø, Sardella, T. C., Brekken, C., Tvedt, K. E., Barnett, S. C., Haraldseth, O., Berry, M. & Sandvig, A. (2012). *NMR Biomed.* **25**, 620–631.
- Schambach, S. J., Bag, S., Schilling, L., Groden, C. & Brockmann, M. A. (2010). *Methods*, **50**, 2–13.
- Schellenberger, E., Haeckel, A., Schoenert, L., Appler, F., Schnorr, J., Taupitz, M. & Hamm, B. (2012). *Mol. Imaging*, **11**, 383–388.
- Schültke, E., Bewer, B., Wysokinski, T., Chapman, D. & Nikkhah, G. (2010). *AIP Conf. Proc.* **1266**, 111–114.
- Serrano-Ruiz, D., Laurenti, M., Ruiz-Cabello, J., López-Cabarcos, E. & Rubio-Retama, J. (2012). *J. Biomed. Mater. Res. B*, **101**, 498–505.
- Stampanoni, M., Groso, A., Isenegger, A., Mikuljan, G., Chen, Q., Meister, D., Lange, M., Betemps, R., Henein, S. & Abela, R. (2007). *AIP Conf. Proc.* **879**, 848–851.
- Staub, F., Baethmann, A., Peters, J., Weigt, H. & Kempski, O. (1990). *J. Cereb. Blood Flow Metab.* **10**, 866–876.
- Stupp, R. *et al.* (2005). *N. Engl. J. Med.* **352**, 987–996.
- Tromba, G. *et al.* (2010). *AIP Conf. Proc.* **1266**, 18–23.